Supplemental Information for

Effects of Lewis Acidic Metal Ions (M) on Oxygen-Atom Transfer Reactivity of Heterometallic Mn_3MO_4 Cubane and $Fe_3MO(OH)$ and $Mn_3MO(OH)$ Clusters

Davide Lionetti,[†] Sandy Suseno,[†] Emily Y. Tsui,[†] Luo Lu,[‡] Troy A. Stich,[‡] Kurtis M. Carsch,[†,§] Robert J. Nielsen,[†,§] William A. Goddard, III,[†,§] R. David Britt,[‡] and Theodor Agapie*[,†]

[†]Division of Chemistry and Chemical Engineering, California Institute of Technology, 1200 East California Boulevard, MC 127-72, Pasadena, California 91125, United States

[‡]Department of Chemistry, University of California, Davis, California 95616, United States

[§]Materials and Process Simulation Center, California Institute of Technology, Pasadena, California 91125, United States

Contents

Structural Reassignment of $[Mn_3MO_2(H)]$ Clusters (M = Na^+, Sr^{2+}, Ca^{2+}, Zn^{2+}, Y^{3+}). As previously reported, modification of the synthetic protocol (including use of iodosobenzene (PhIO) in place of potassium superoxide as oxygen atom transfer agent) enables access to tetrametallic clusters incorporating two oxygen atoms (**$[Mn^{III}_3MO(OH)]$**, **$[Mn^{II}Mn^{III}_2MO(OH)]$**, Figure 1). These complexes were obtained from the same **$LMn^{II}_3(OAc)_3$** precursor used for preparing $[Mn_3MO_4]$ cubane clusters.[1] Structural characterization of these materials by XRD revealed tetrametallic clusters containing a μ_4-oxo ligand. A second oxygen atom was incorporated as a μ_2-bridge between the apical (redox-inactive) metal and one of the basal Mn centers. The oxidation states of the three Mn centers in these clusters were originally assigned, based a combination of magnetic susceptibility, XRD, and XAS data, as **$[Mn^{III}_2Mn^{IV}MO_2]$** and **$[Mn^{III}_3MO_2]$** clusters. This interpretation of the available data led to assignment of the μ_2-bridges as oxo (O^{2-}) moieties based on charge balance in the overall structures.

Although these measurements were consistent with the one-electron change in redox state, assignment of the absolute oxidation states remained inconclusive.[1] Subsequently, the isostructural Fe_3 clusters (**$[Fe^{III}_3MO(OH)]$**, **$[Fe^{II}Fe^{III}_2MO(OH)]$**, Figure 1), were prepared and the μ_2 bridging moiety was conclusively identified as a hydroxo (HO^-) ligand.[2] The Fe oxidation states in Fe_3 clusters were unambiguously determined via Mössbauer spectroscopy as Fe^{III}_3 and $Fe^{III}_2Fe^{II}$ in complexes **$[Fe^{III}_3MO(OH)]$** and **$[Fe^{II}Fe^{III}_2MO(OH)]$**, respectively. The hydroxide assignment was derived from charge-balance of the XRD structures. Comparison of the structural metrics of Fe_3 and Mn_3 clusters show elongation of a single M–(μ_4-O) bond in reduced complexes **$[Fe^{II}Fe^{III}_2MO(OH)]$** and the Mn analog, initially assigned as Mn^{III}_3M (Table S1), suggesting the presence of a single reduced Mn center as $Mn^{II}Mn^{III}_2M$ clusters, and therefore supporting assignment of Mn oxidation states in the oxidized and reduced Mn clusters as Mn^{III}_3 and $Mn^{III}_2Mn^{II}$, respectively. Thus, by charge-balance of the solid-state structure, the μ_2 bridging moiety is assigned as OH^- as in the Fe_3 clusters resulting in reassigned complexes as **$[Mn^{III}_3MO(OH)]$** and **$[Mn^{II}Mn^{III}_2MO(OH)]$**.

Density functional theory (DFT) calculations were carried out to further corroborate the structural reassignment of complexes **$[Mn^{III}_3MO(OH)]$** and **$[Mn^{II}Mn^{III}_2MO(OH)]$**. Clusters **$[Mn^{III}_3CaO(OH)]$** and **$[Mn^{II}Mn^{III}_2CaO(OH)]$** were modeled using Jaguar 8.4[3] (see page S6 for the full computational protocol) both as originally assigned–$[Mn^{III}_2Mn^{IV}CaO_2]$ (**oxCa'**) and $[Mn^{III}_3CaO_2]$ (**redCa'**), respectively–and also according to the new structural assignment proposed herein–$[Mn^{III}_3CaO(OH)]$ (**oxCa"**) and $[Mn^{II}Mn^{III}_2CaO(OH)]$ (**redCa"**). Selected bond metrics for the optimized structures as well as the values observed experimentally (XRD) are shown in Table S3. For both oxidized and reduced complexes, modeling of the clusters as the more reduced oxo-hydroxo species provides structural parameters in closer agreement with the experimental values than those calculated for the more oxidized dioxo clusters. In particular, the Mn(1)–O(2) distance, which is expected to be sensitive to the nature of the μ_2-ligand, is calculated to be considerably shorter for clusters containing a μ_2-O^{2-} ligand (1.683 Å and 1.697 Å for **oxCa'** and **redCa'**, respectively) than for hydroxide-bridged clusters (1.830 Å and 1.907 Å for **oxCa"** and **redCa"**, respectively). The experimental values (1.842(3) Å and 1.887(3) Å) agree more closely with the bond distances from the computational studies, supporting the assignment of **$[Mn^{III}_3CaO(OH)]$** and **$[Mn^{II}Mn^{III}_2CaO(OH)]$** as oxo-hydroxo clusters.

The new structural assignment for clusters **$[Mn^{III}_3MO(OH)]$** and **$[Mn^{II}Mn^{III}_2MO(OH)]$**, is further supported by electron paramagnetic resonance (EPR) spectroscopy. Normal-mode X-band EPR characterization obtained in CH_2Cl_2 glass at cryogenic temperatures revealed weak

signals for **[Mn^{III}_3CaO(OH)]** and **[Mn^{III}_3SrO(OH)]** (Figure S1a and S2a), consistent with integer-spin systems, and more intense signals for **[$Mn^{II}Mn^{III}_2$CaO(OH)]** and **[$Mn^{II}Mn^{III}_2$SrO(OH)]** (Figure S1b and S2b), consistent with half-integer systems. These observations are inconsistent with the original oxidation state assignment for these clusters: a $Mn^{III}_2Mn^{IV}$M complex would be a half-integer spin system (d^4, d^4, d^3), whereas a Mn^{III}_3M species would be an integer-spin system (d^4, d^4, d^4). The EPR data is consistent with the newly proposed assignments of **[Mn^{III}_3MO(OH)]** as [Mn^{III}_3] (d^4, d^4, d^4, an integer-spin system) and of **[$Mn^{II}Mn^{III}_2$MO(OH)]** as [$Mn^{III}_2Mn^{II}$] (d^4, d^4, d^5, a half-integer spin system). It should be noted that the changes in assignment of the oxidation states and identity of bridging ligands in clusters **[Mn^{III}_3MO(OH)]** and **[$Mn^{II}Mn^{III}_2$MO(OH)]** bear no effect on the conclusions of earlier studies on these complexes regarding the effect of the redox inactive metal on reduction potentials.[1] All comparisons within this series of complexes remain valid, as changes affect compounds across the entire series. The reactivity studies described next were focused on the available oxo-hydroxo complexes.

Table S1. Bond Parameters (Measured in Å) from Computation

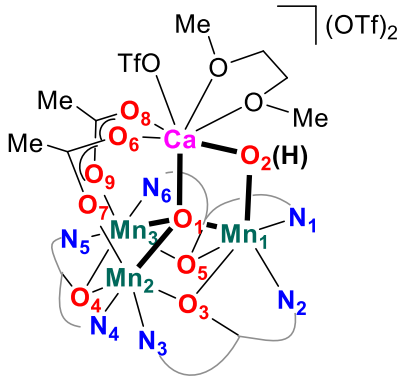

Bond	oxCa (XRD)[1]	oxCa'	oxCa''	redCa (XRD)[1]	redCa'	redCa''	redCa''-noH
Mn2–N4	2.095	2.122	2.140	2.089	2.176	2.278	2.277
Mn2–N3	2.241	2.292	2.251	2.341	2.264	2.254	2.341
Mn2–O3	1.884	1.908	1.893	1.936	1.876	2.101	2.106
Mn2–O4	2.265	2.224	2.248	2.111	2.281	2.282	2.262
Mn2–O7	1.913	1.922	1.906	1.971	1.922	2.096	2.094
Mn2–O1	1.913	1.889	1.918	2.159	1.906	2.203	2.195
Mn3–N5	2.161	2.107	2.255	2.290	2.287	2.256	2.194
Mn3–N6	2.124	2.166	2.125	2.205	2.142	2.219	2.170
Mn3–O5	2.232	2.226	2.379	2.322	2.149	2.308	2.397
Mn3–O4	1.872	1.857	1.911	2.092	1.935	1.939	1.910
Mn3–O9	1.910	1.896	1.867	2.129	1.938	1.928	1.884
Mn3–O1	2.017	2.054	1.944	1.939	1.848	1.827	1.907
Mn1–N1	2.170	2.208	2.161	2.211	2.151	2.278	2.303
Mn1–N2	2.129	2.145	2.143	2.156	2.187	2.131	2.159
Mn1–O3	2.215	2.279	2.261	2.250	2.281	2.142	2.178
Mn1–O5	1.878	1.908	1.896	1.900	2.029	1.941	1.912
Mn1–O1	1.958	1.972	2.006	1.860	2.141	1.958	1.894
Mn1–O2	1.842	1.683	1.830	1.887	1.697	1.837	1.907
Ca1–O1	2.452	2.445	2.479	2.397	2.474	2.424	2.410
Ca1–O2	2.349	2.556	2.422	2.368	2.394	2.389	2.504
O2–OTf	(2.847)[a]	--	2.692	2.742	--	2.664	--

[a] distance between O2 and H-bonded 1,2-dimethoxyethane (DME) solvent molecule

Calculation of Mulliken Spin Populations

Mulliken population analysis was employed to assign oxidation states of all atoms based on the number of unpaired spins. The bridging alkoxides exhibited α spins on the order of ~ 0.10 due to the highly covalent Mn-O bonds. Spin on the remaining scaffold was found to be negligible (< 0.02 α spins per remaining atoms). For **redCa''**, Mulliken spin population revealed an alternative oxidation state assignment in which Mn2 is assigned as Mn(II) as Mn3 is assigned as Mn(III).

Table S2. Mulliken Spin Populations.

Atom	oxCa'	oxCa''	redCa'	redCa''	redCa''-noH
Mn1	3.49	3.83	3.72	3.82	3.85
Mn2	3.87	3.87	3.88	3.86	3.87
Mn3	3.86	3.88	3.84	4.82	4.81
Ca1	0.01	0.00	0.00	0.00	0.00
O1	0.00	0.00	0.00	0.00	0.00
O2	-0.61	0.00	0.18	0.00	0.00

Table S3. Comparison of Selected Bond Distances (in Å) for Complexes $[Fe^{III}_3CaO(OH)]$ (oxFe), $[Fe^{II}Fe^{III}_2CaO(OH)]$ (redFe), $[Mn^{III}_3CaO(OH)]$ (oxCa), $[Mn^{II}Mn^{III}_2CaO(OH)]$ (redCa) (XRD), oxCa', oxCa'', redCa', and redCa'' (DFT).

Bond	oxFe (XRD)	redFe (XRD)	oxCa (XRD)	redCa (XRD)	oxCa' (DFT)	oxCa'' (DFT)	redCa' (DFT)	redCa'' (DFT)
M_1–O_1	2.023(2)	1.928(5)	1.958(3)	1.860(3)	1.972	2.006	2.141	1.894
M_2–O_1	1.927(2)	1.904(5)	1.913(3)	2.159(3)	1.889	1.918	1.906	2.195
M_3–O_1	1.945(2)	2.140(5)	2.017(3)	1.939(3)	2.054	1.944	1.848	1.907
M_1–O_2	1.881(2)	1.923(5)	1.842(3)	1.887(3)	1.683	1.830	1.697	1.907

EPR Spectroscopy

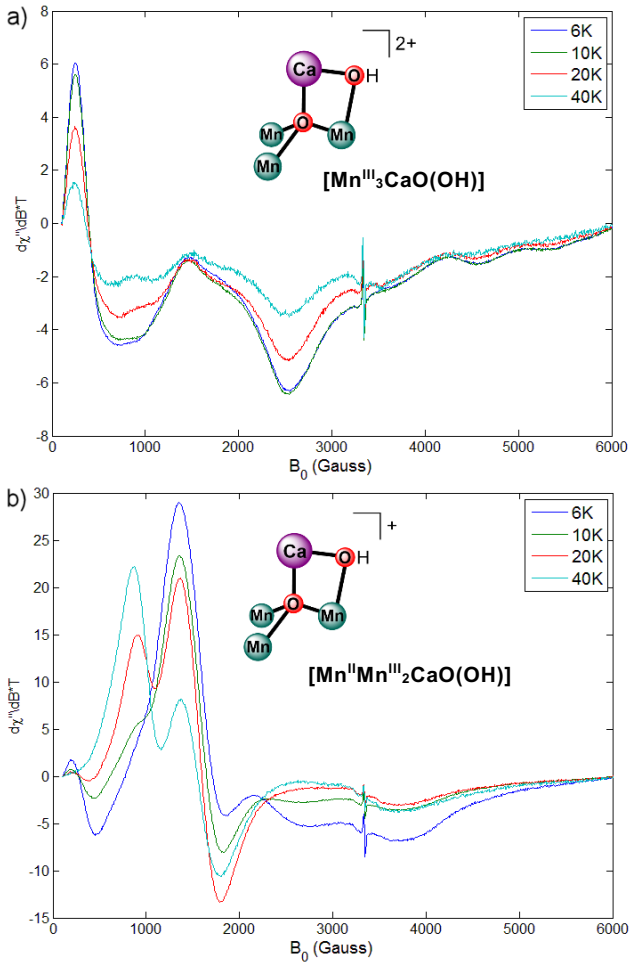

Figure S1. Temperature-dependent CW X-Band EPR perpendicular-mode spectra of the frozen solutions of (a) **[Mn$^{III}_3$CaO(OH)]** and (b) **[Mn^{II}Mn$^{III}_2$CaO(OH)]** dissolved in dichloromethane. Experimental parameters: microwave frequency = 9.36–9.38 GHz; power = 0.07962 mW for (a) and 0.1589 mW for (b); modulation amplitude = 10.0 G; modulation frequency = 100 kHz.

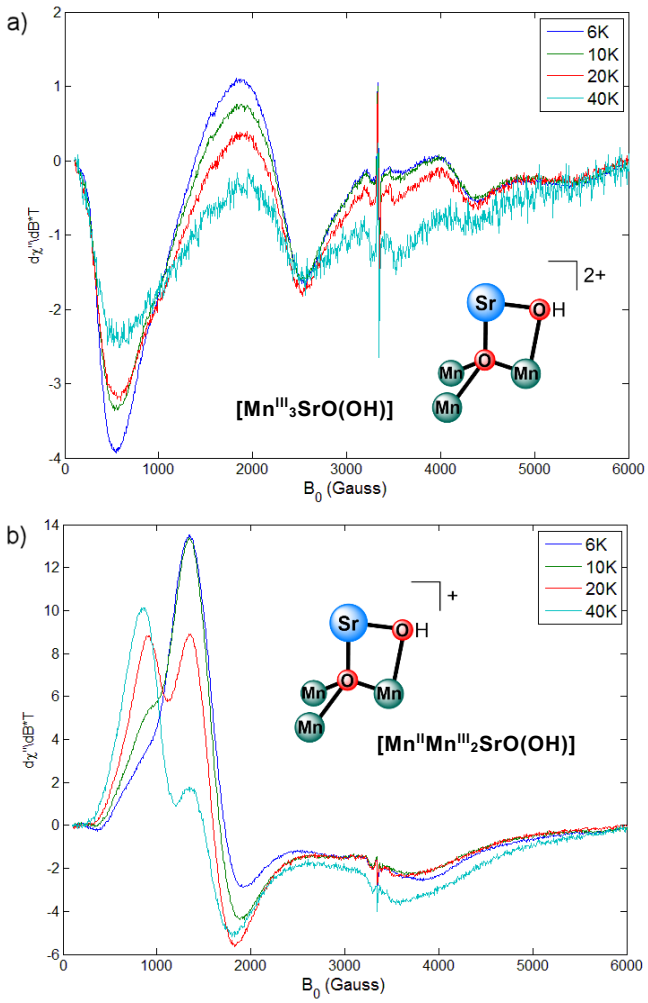

Figure S2. Temperature-dependent CW X-Band EPR perpendicular-mode spectra of the frozen solutions of (a) **[Mn$^{III}_3$SrO(OH)]** and (b) **[Mn^{II}Mn$^{III}_2$SrO(OH)]** dissolved in dichloromethane. Experimental parameters: microwave frequency = 9.36–9.38 GHz; power = 0.07962 mW for (a) and 0.1589 mW for (b); modulation amplitude = 10.0 G; modulation frequency = 100 kHz.

NMR Spectroscopy

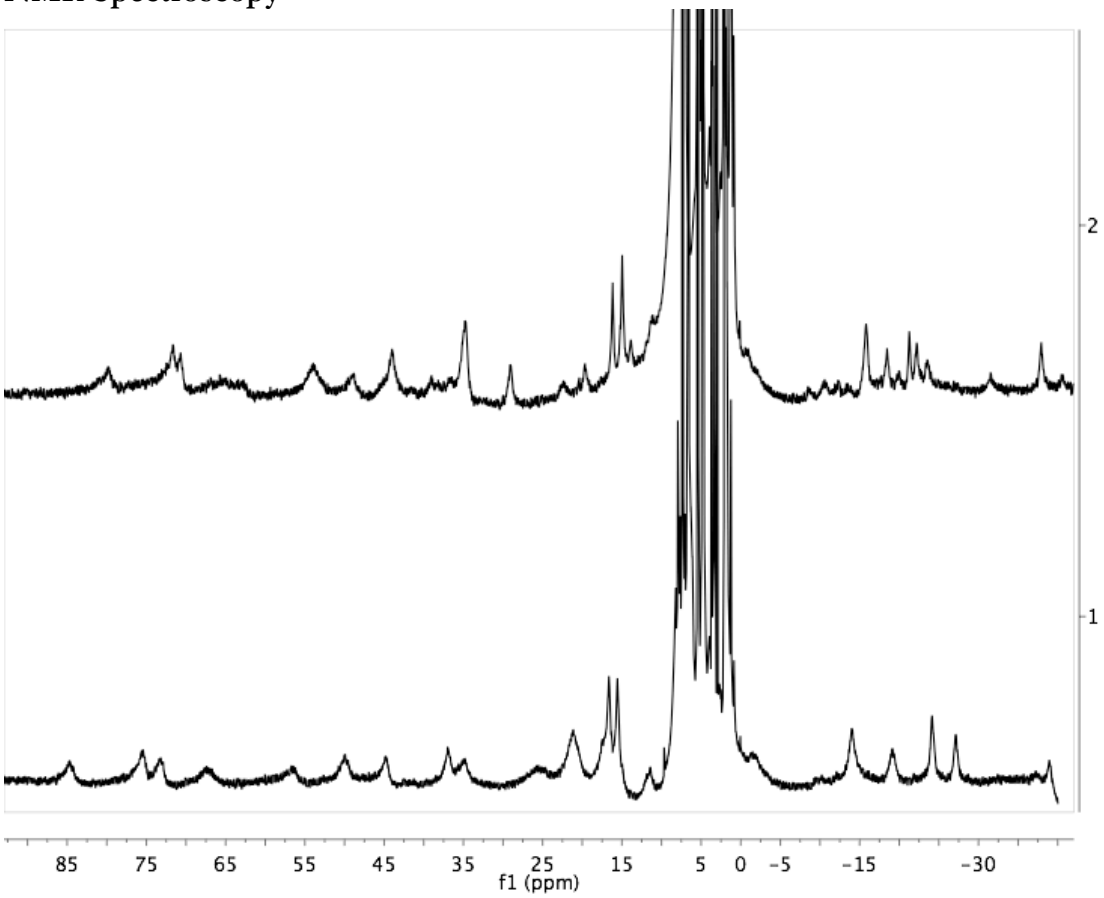

Figure S3. (*Top*) ^{1}H NMR (300 MHz, CD_2Cl_2) spectrum of the intermediate species formed from the reaction of **[$Mn^{II}Mn^{III}_2YO(OH)$]** with 10 equiv. PPh_3 within 30 mins. (*Bottom*) ^{1}H NMR (300 MHz, CD_3CN) spectrum $[LCaMn_3O(OTf)_2(OAc)_3]_2$ dimer.[4]

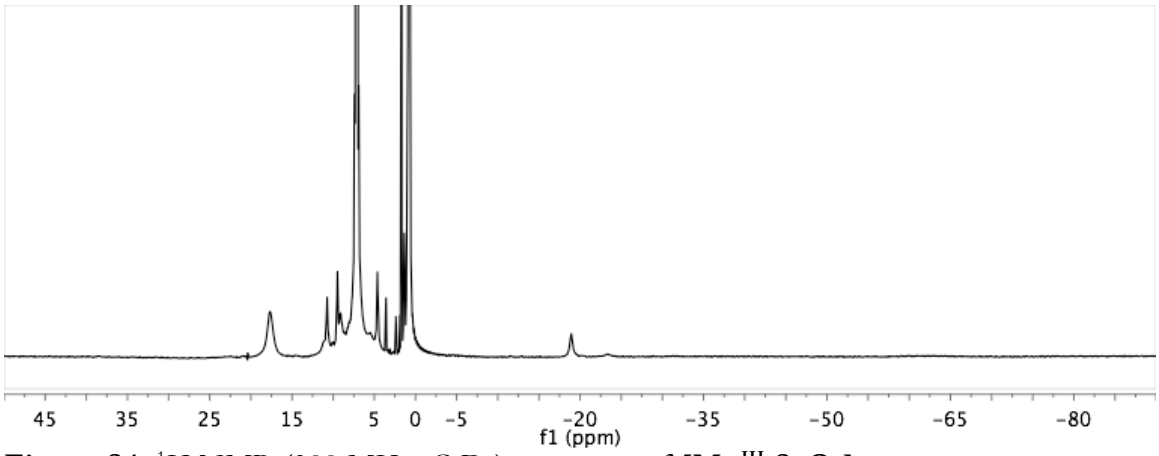

Figure S4. ^{1}H NMR (300 MHz, C_6D_6) spectrum of **[$Mn^{III}_3ScO_3$]**.

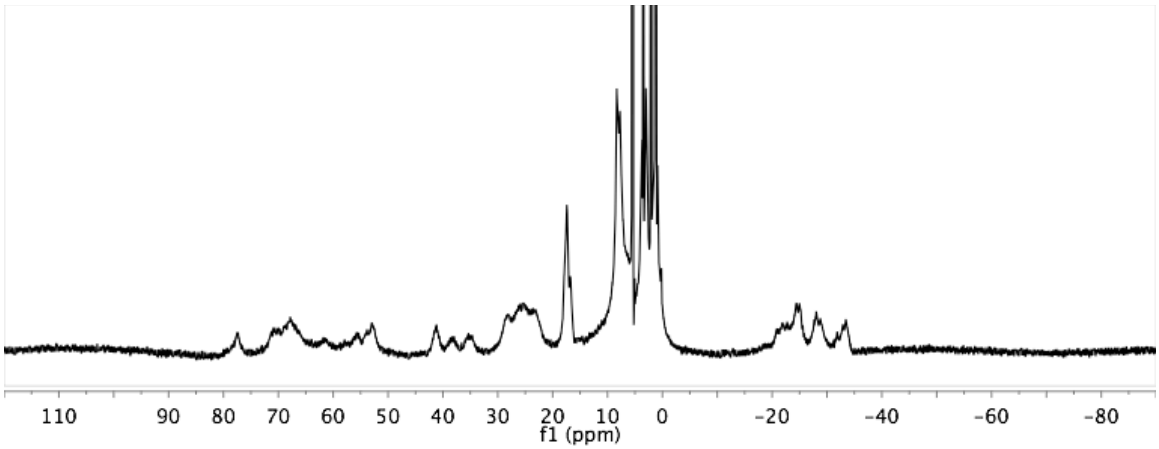

Figure S5. ^{1}H NMR (300 MHz, CD_2Cl_2) spectrum of **[$Mn^{III}_3YO(OH)]_2$**.

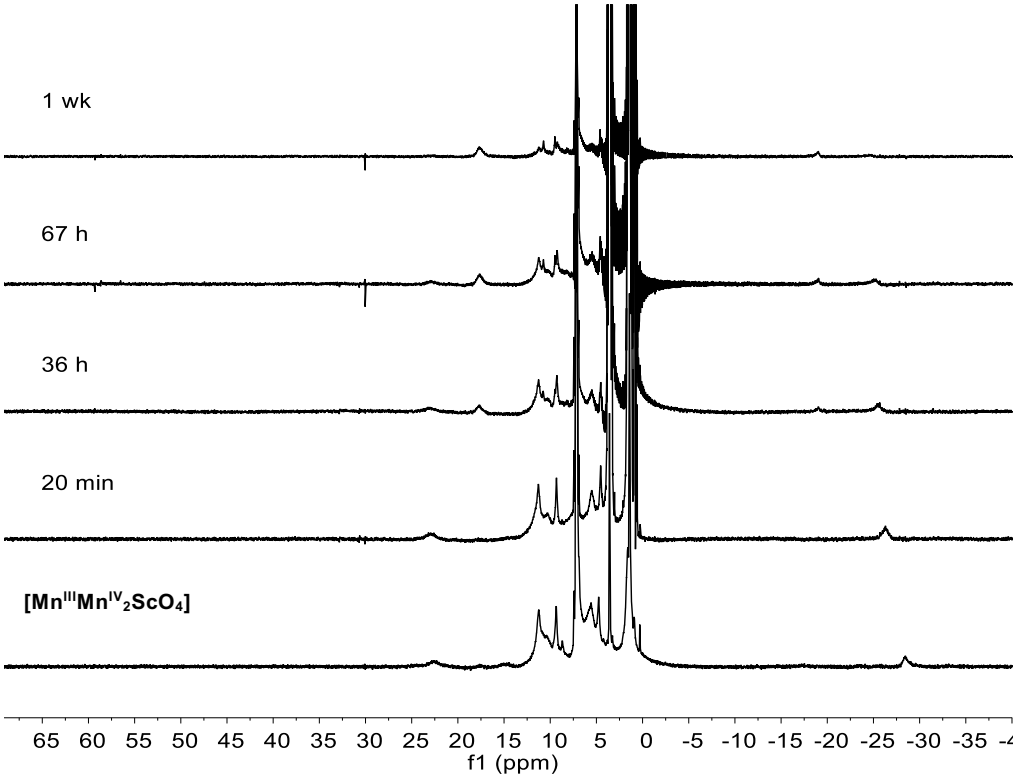

Figure S6. ^{1}H NMR (300 MHz, C_6D_6) of reaction of **[$Mn^{III}Mn^{IV}_2ScO_4$]** with PMe_3 (10 equiv).

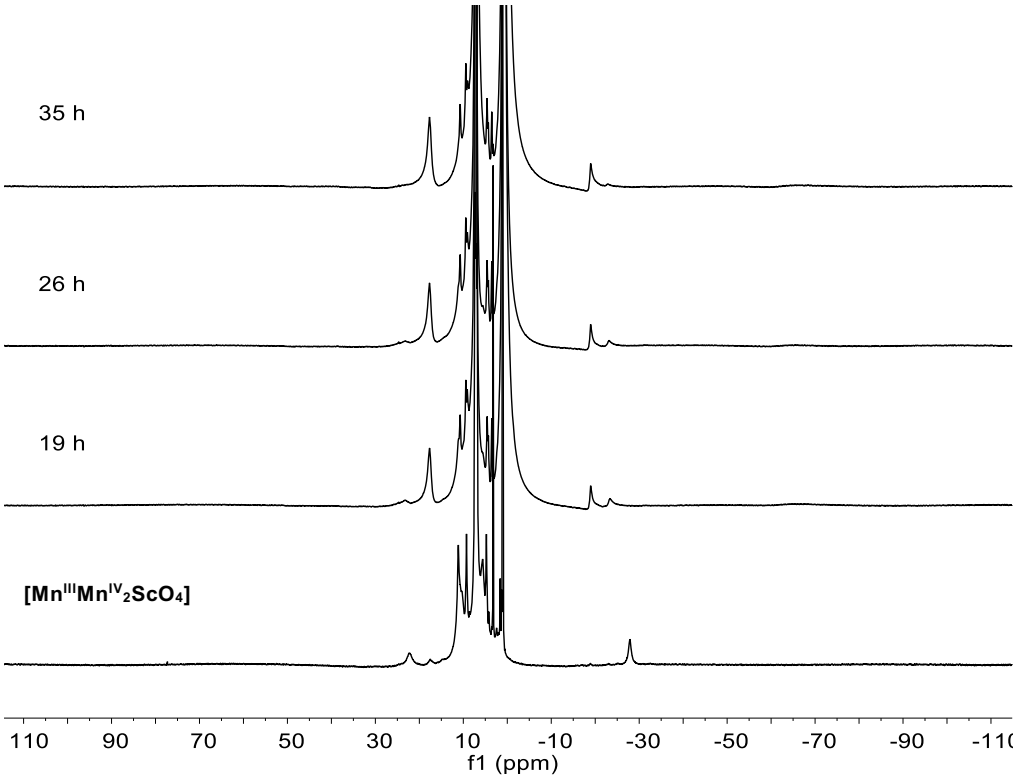

Figure S7. ^{1}H NMR (300 MHz, C_6D_6) of reaction of **[$Mn^{III}Mn^{IV}_2ScO_4$]** with PMe_3 (10 equiv) at 50 °C.

Figure S8. ^{1}H NMR (300 MHz, C_6D_6) of reaction of **[$Mn^{III}Mn^{IV}_2GdO_4$]** with PMe_3 (10 equiv) at room temperature.

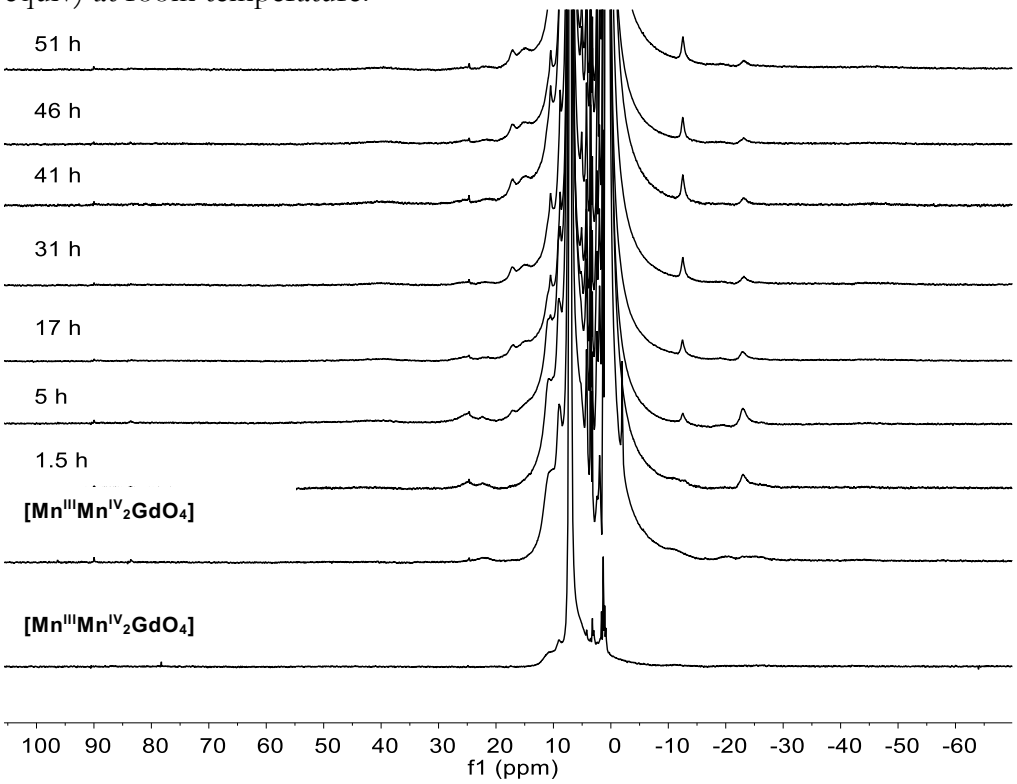

Figure S9. ^{1}H NMR (300 MHz, C_6D_6) of reaction of **[$Mn^{III}Mn^{IV}_2GdO_4$]** with PMe_3 (10 equiv) at 50 °C.

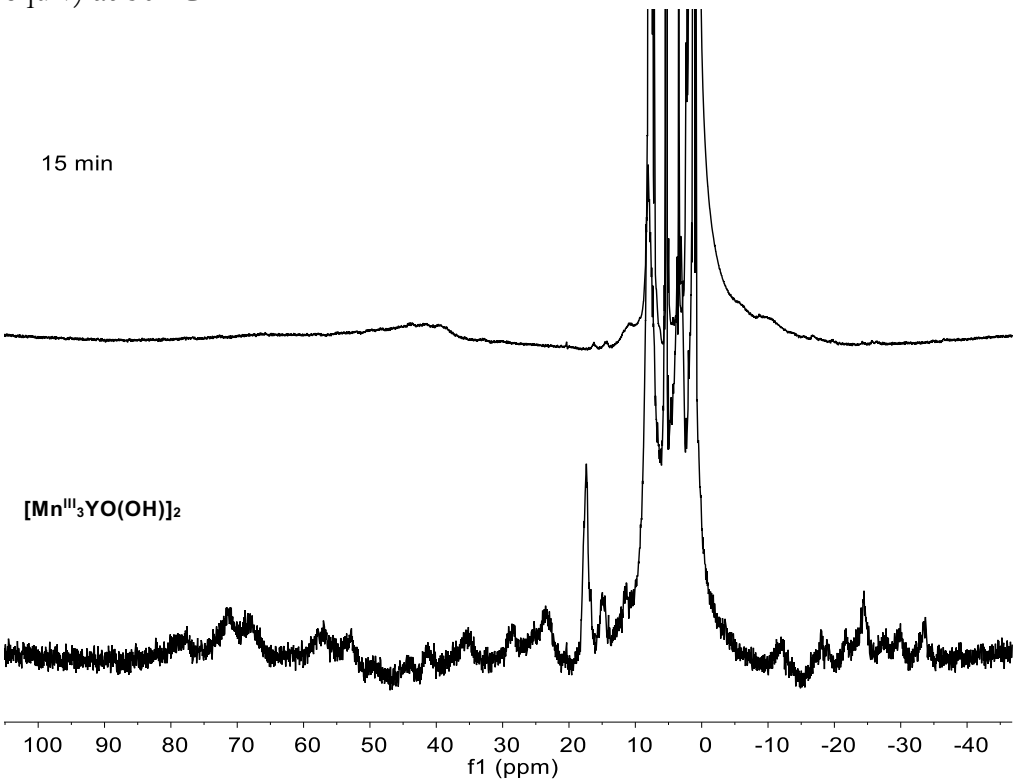

Figure S10. ^{1}H NMR (300 MHz, CD_2Cl_2) of reaction of **[$Mn^{III}_3YO(OH)]_2$** with PEt_3 (10 equiv).

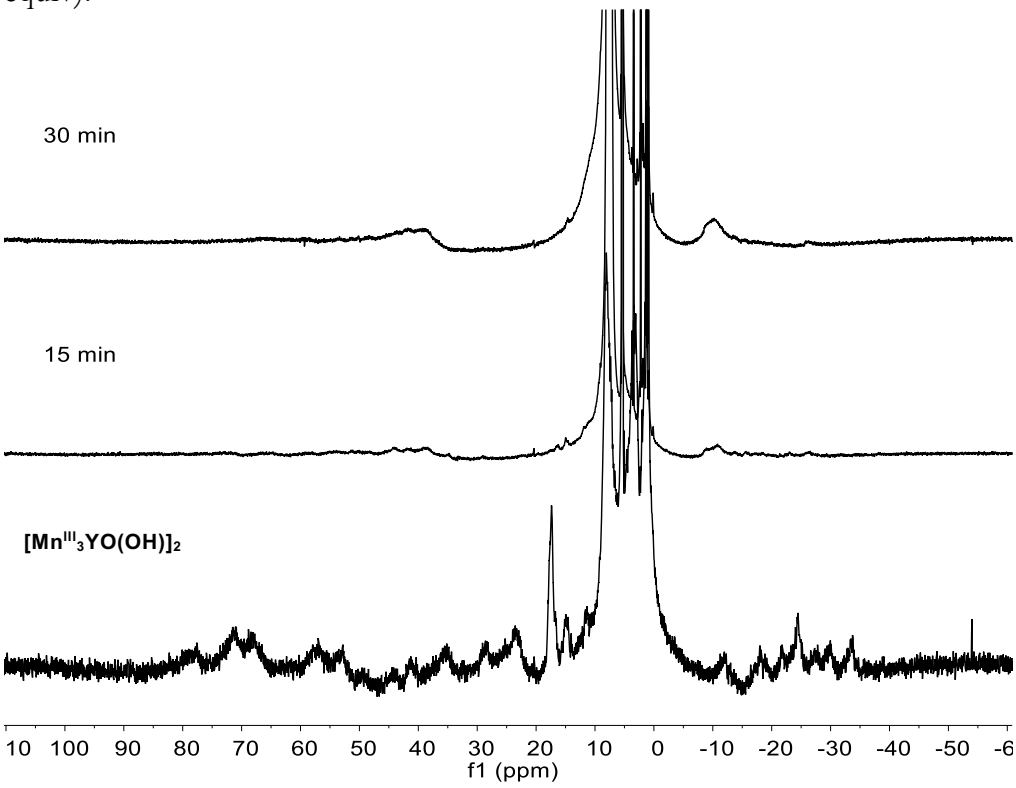

Figure S11. ^{1}H NMR (300 MHz, CD_2Cl_2) of reaction of **$[Mn^{III}_3YO(OH)]_2$** with PPh_3 (10 equiv).

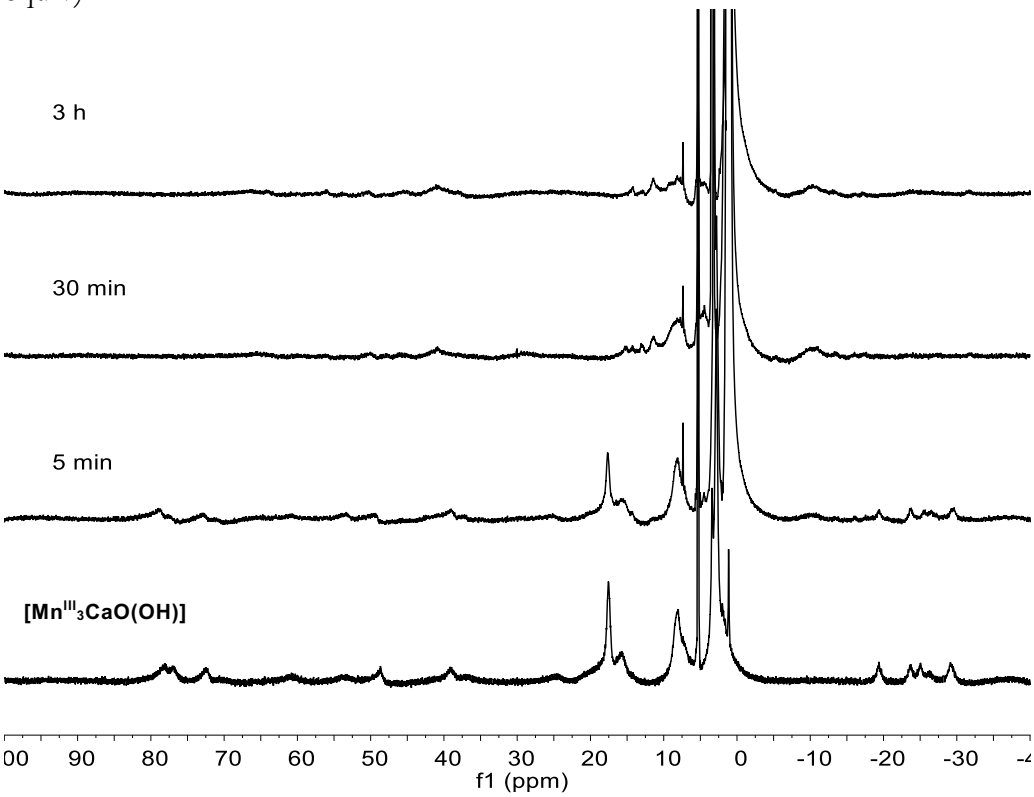

Figure S12. ^{1}H NMR (300 MHz, CD_2Cl_2) of reaction of **$[Mn^{III}_3CaO(OH)]$** with PEt_3 (10 equiv).

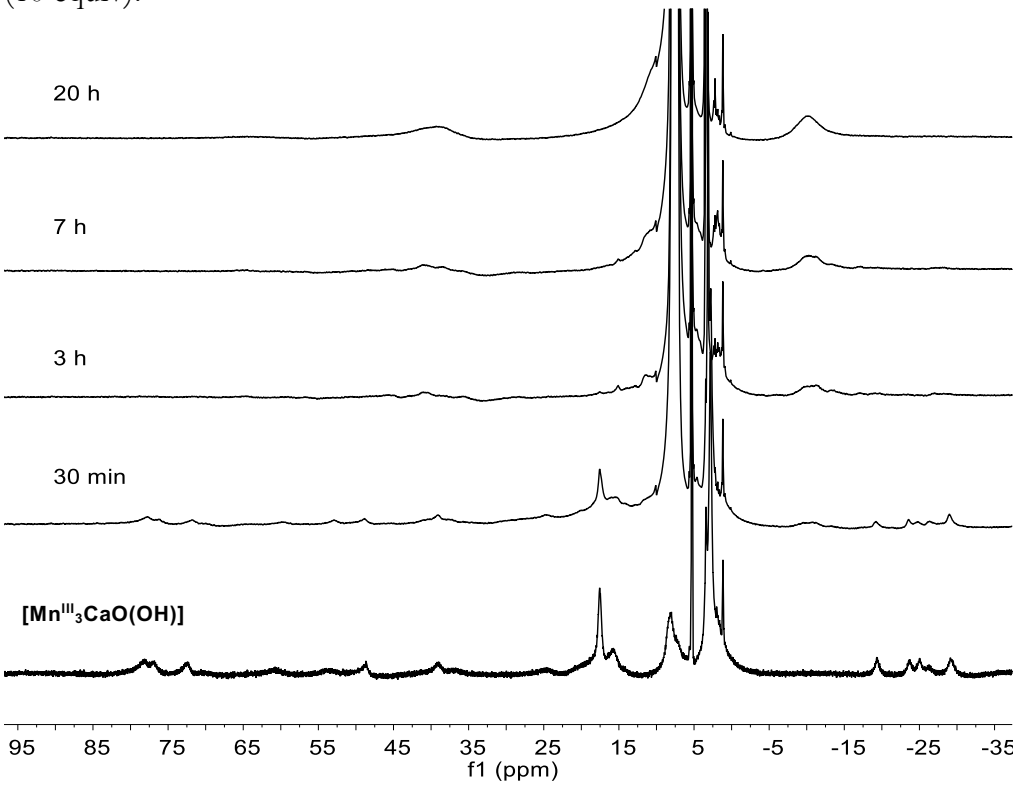

Figure S13. ^{1}H NMR (300 MHz, CD_2Cl_2) of reaction of **[$Mn^{III}_3CaO(OH)$]** with PPh_3 (10 equiv).

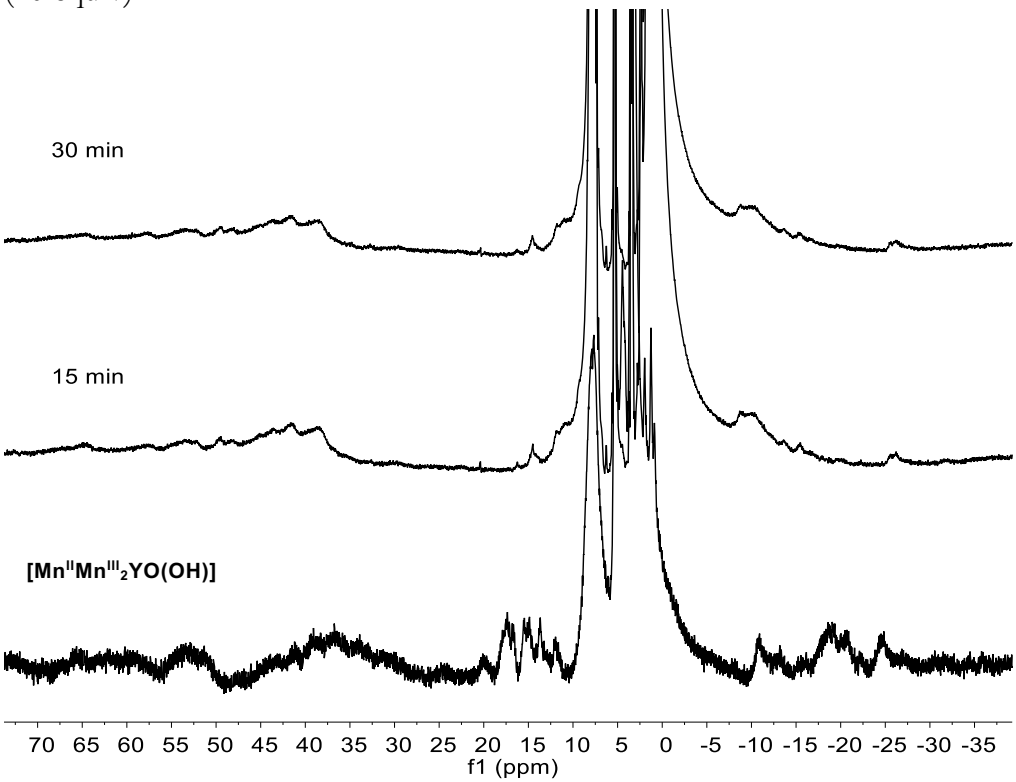

Figure S14. ^{1}H NMR (300 MHz, CD_2Cl_2) of reaction of **[$Mn^{II}Mn^{III}_2YO(OH)$]** with PEt_3 (10 equiv).

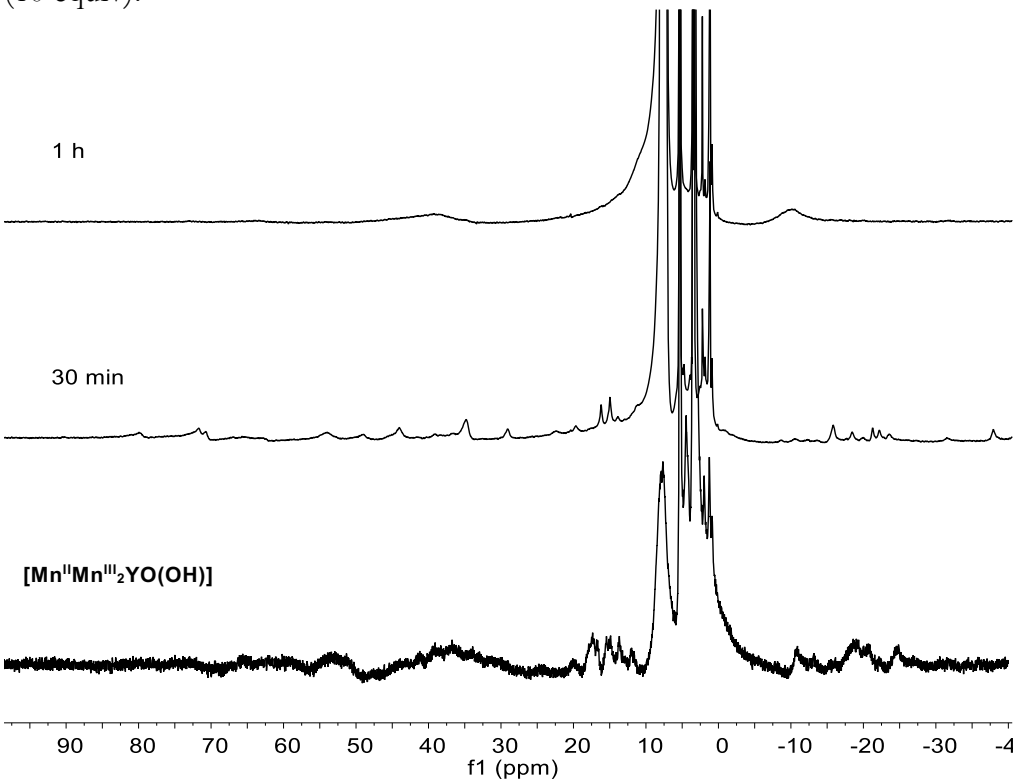

Figure S15. ^{1}H NMR (300 MHz, CD_2Cl_2) of reaction of **[$Mn^{II}Mn^{III}_2YO(OH)$]** with PPh_3 (10 equiv).

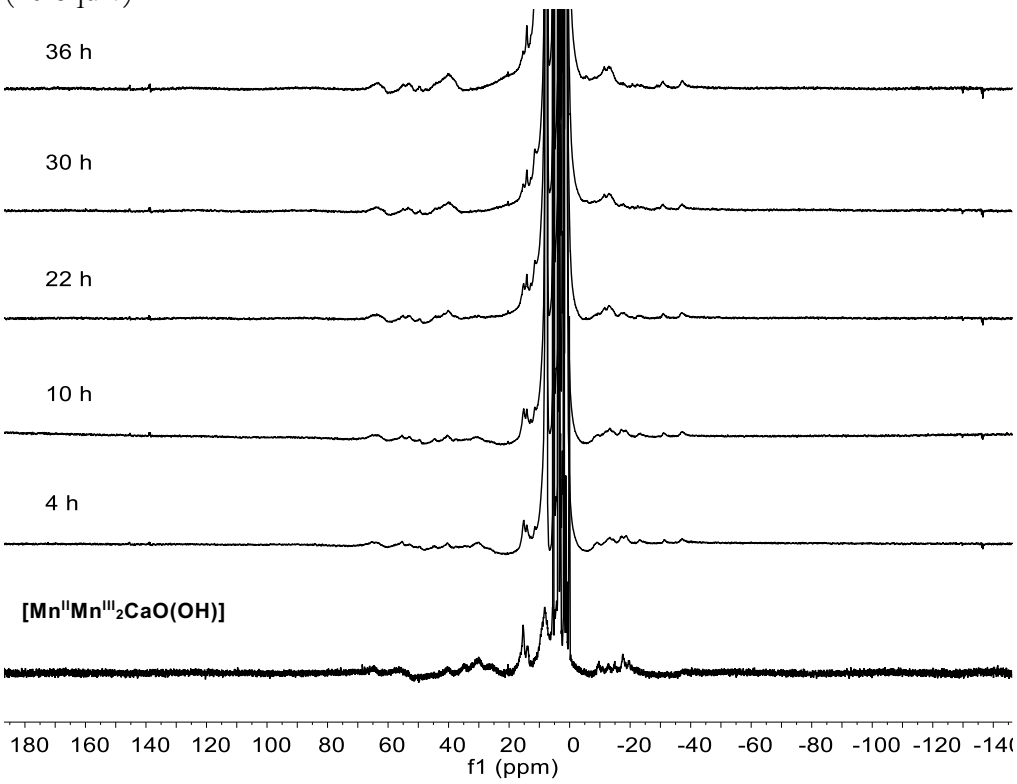

Figure S16. ^{1}H NMR (300 MHz, CD_2Cl_2) of reaction of **[$Mn^{II}Mn^{III}_2CaO(OH)$]** with PEt_3 (10 equiv).

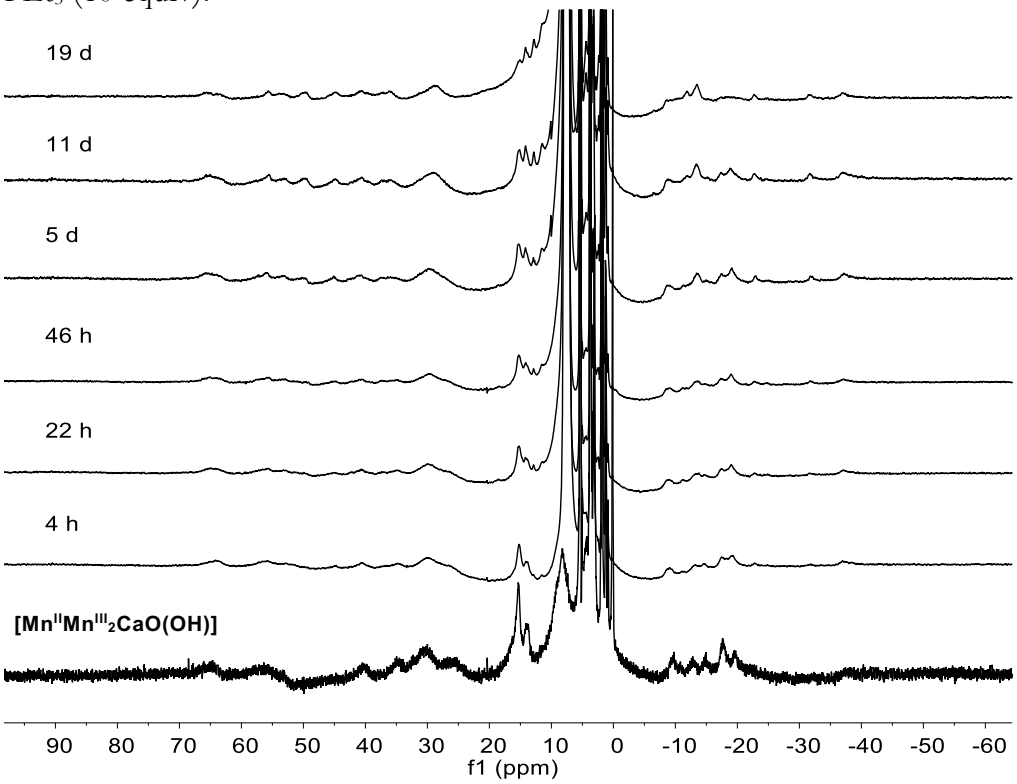

Figure S17. ^{1}H NMR (300 MHz, CD_2Cl_2) of reaction of **[$Mn^{II}Mn^{III}_2CaO(OH)$]** with PPh_3 (10 equiv).

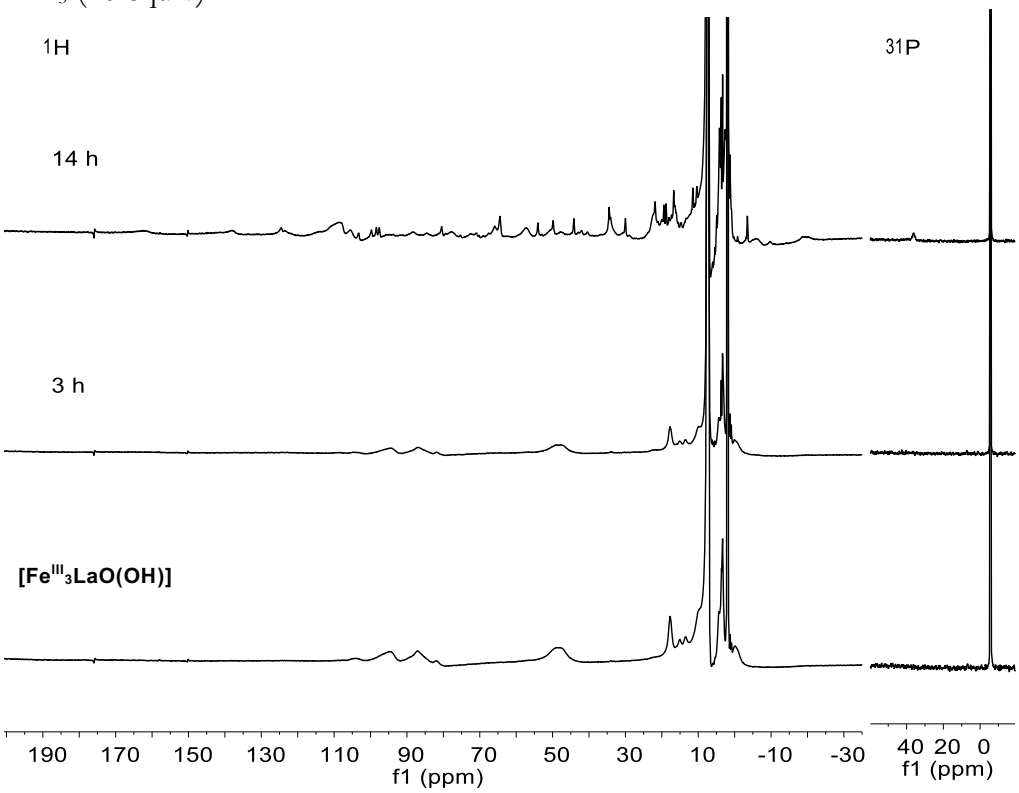

Figure S18. ^{1}H NMR (300 MHz, CD_3CN) and ^{31}P NMR (121 MHz) of reaction of **[$Fe^{III}_3LaO(OH)$]** with PPh_3 (10 equiv).

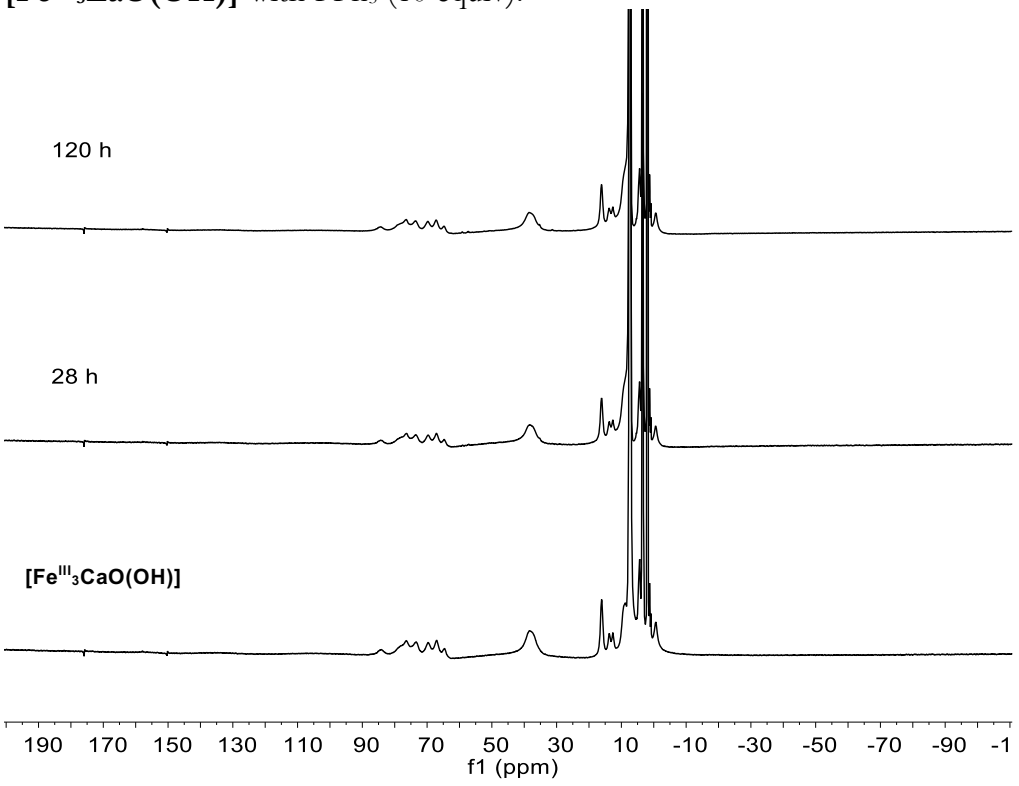

Figure S19. ^{1}H NMR (300 MHz, CD_3CN) of reaction of **[$Fe^{III}_3CaO(OH)$]** with PPh_3 (10 equiv).

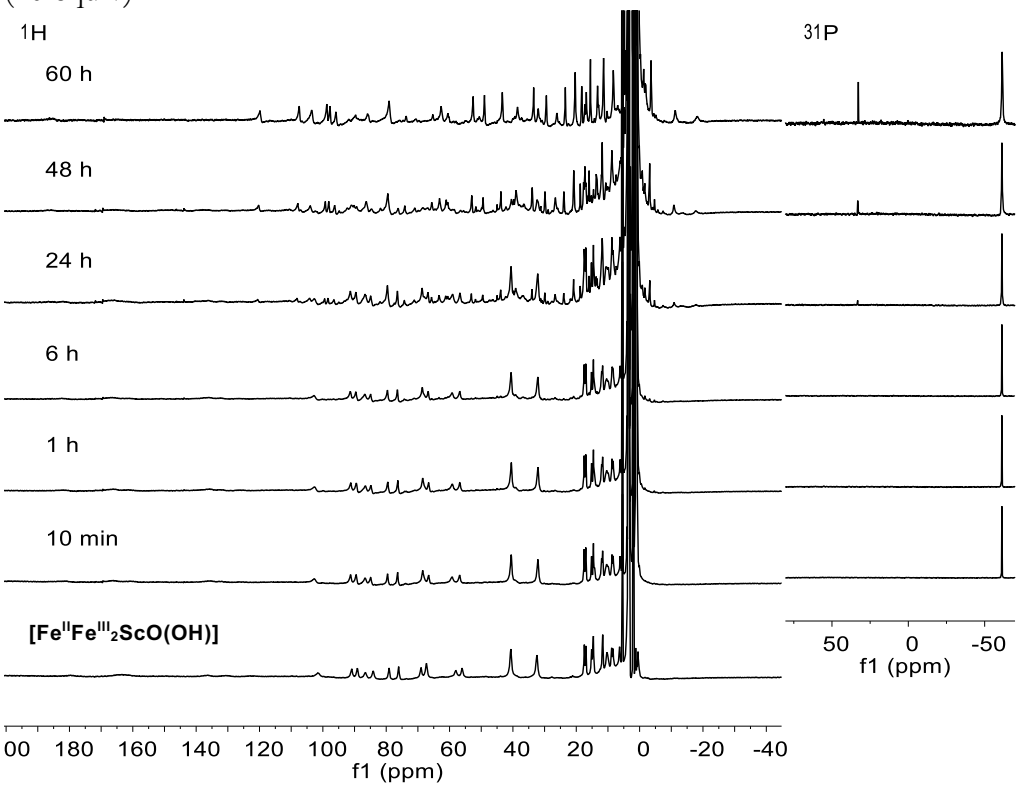

Figure S20. ^{1}H NMR (300 MHz, 1:1 CD_3CN/CD_2Cl_2) and ^{31}P NMR (121 MHz) of reaction of **[$Fe^{II}Fe^{III}_2ScO(OH)$]** with PMe_3 (10 equiv).

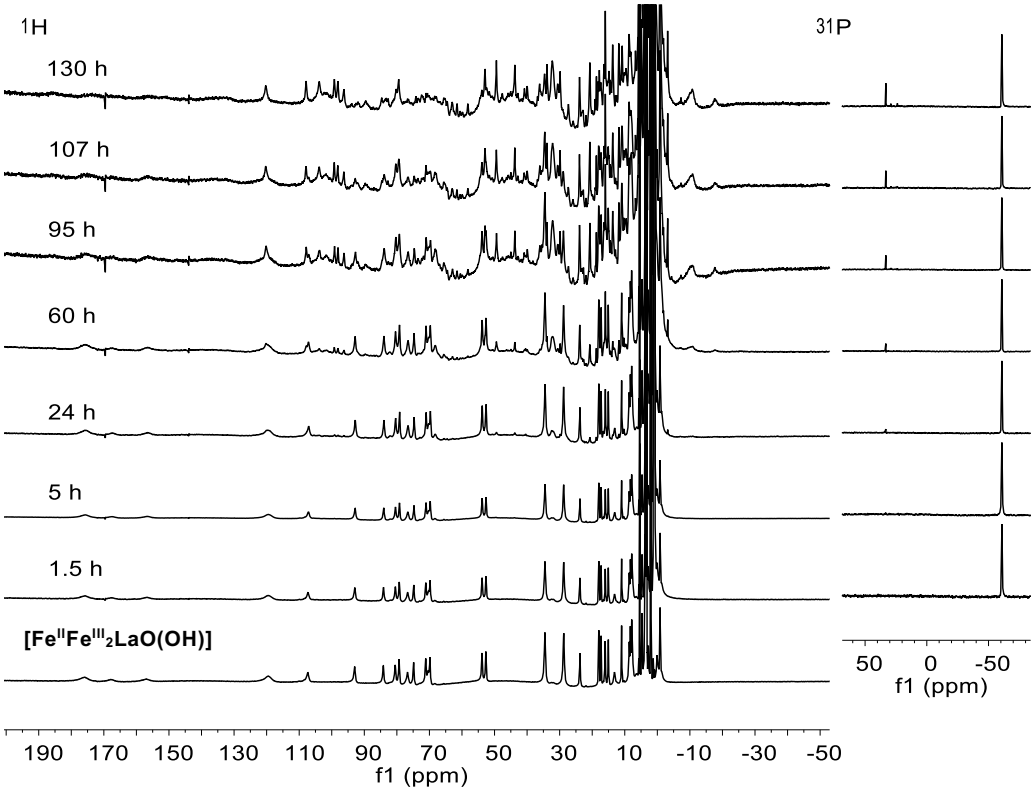

Figure S21. ^{1}H NMR (300 MHz, C_6D_6) and ^{31}P NMR (121 MHz) of reaction of **[$Fe^{II}Fe^{III}_2$LaO(OH)]** with PMe_3 (10 equiv).

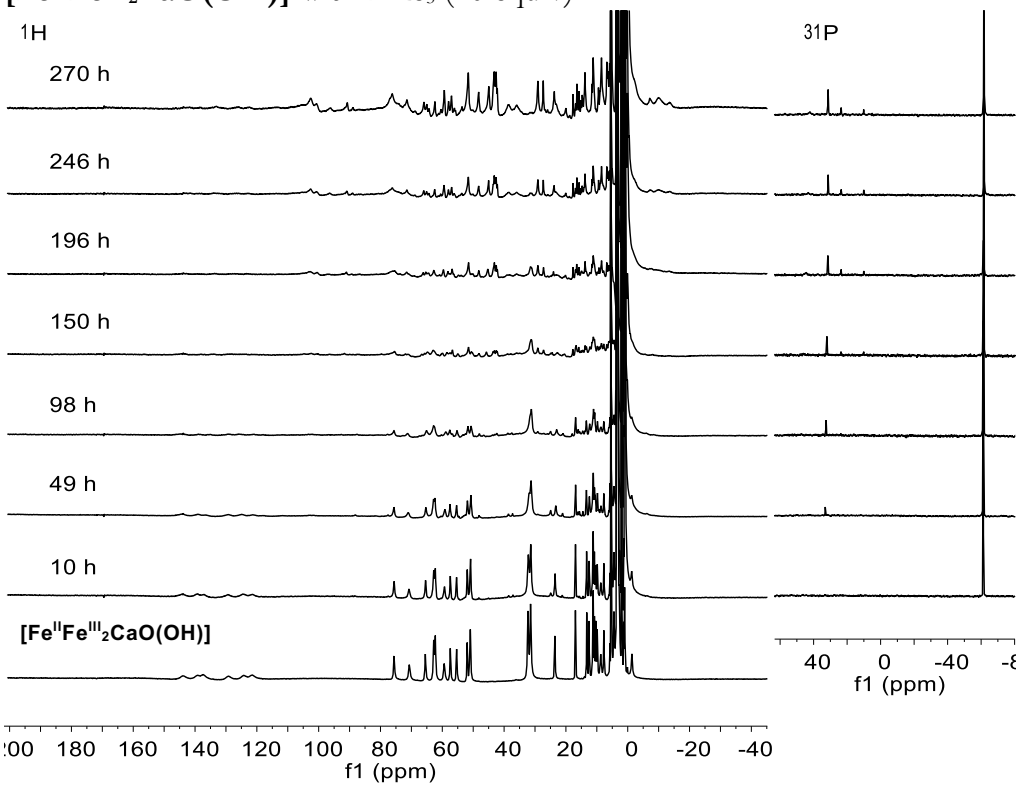

Figure S22. ^{1}H NMR (300 MHz, C_6D_6) and ^{31}P NMR (121 MHz) of reaction of **[$Fe^{II}Fe^{III}_2$CaO(OH)]** with PMe_3 (10 equiv).

Crystallographic Information.

CCDC 1035222 (**[$Mn^{III}_3ScO_3$]**) contains the supporting crystallographic data for this paper. These data can be obtained free of charge from The Cambridge Crystallographic Data Centre via www.ccdc.cam.ac.uk/data_request/cif.

Refinement details

In each case, crystals were mounted on a glass fiber or nylon loop using Paratone oil, then placed on the diffractometer under a nitrogen stream. Low temperature (100 K) X-ray data were obtained on a Bruker APEXII CCD based diffractometer (Mo sealed X-ray tube, K_α = 0.71073 Å). All diffractometer manipulations, including data collection, integration, and scaling, were carried out using the Bruker APEXII software.[5] Absorption corrections were applied using SADABS.[6] Space groups were determined on the basis of systematic absences and intensity statistics and the structures were solved by direct methods using XS[7] (incorporated into SHELXTL)[8] and refined by full-matrix least squares on F^2. All non-hydrogen atoms were refined using anisotropic displacement parameters. Hydrogen atoms were placed in idealized positions and refined using a riding model. The structure was refined (weighted least squares refinement on F^2) to convergence. Due to the size of the compound, most crystals included solvent accessible voids, which tended to contain disordered solvent. In addition, due to a tendency to desolvate, the long range order of these crystals and amount of high angle data we were able to record was in some cases not ideal. These disordered solvent molecules were largely responsible for the alerts generated by the checkCIF protocol.

Table S4. Crystal and refinement data for complex **[$Mn^{III}_3ScO_3$]**

	[$Mn^{III}_3ScO_3$]
empirical formula	C_{82} H_{74} Mn_3 N_6 $O_{14.14}$ Sc
formula wt	1579.44
T (K)	100
a, Å	12.2754(13)
b, Å	15.4073(17)
c, Å	20.687(2)
α, deg	85.434(6)
β, deg	72.878(6)
γ, deg	76.278(6)
V, $Å^3$	3632.1(7)
Z	2
Cryst. system	Triclinic
Space group	P–1
d_{calcd}, g/cm^3	1.444
θ range, deg	1.698 – 30.666
μ, mm^{-1}	0.670
abs cor	Semi-empirical from equivalents
GOF[c]	1.080
R1,[a] wR2[b] (I > 2σ(I))	0.0608, 0.1283

[a]$R1 = \Sigma||F_o|-|F_c|| / \Sigma|F_o|$ [b] $wR2 = \# \Sigma [w(F_o^2-F_c^2)^2] / \Sigma [w(F_o^2)^2] \#^{1/2}$ [c] $GOF = S = \# \Sigma [w(F_o^2-F_c^2)^2] / (n-p) \#^{1/2}$

Special refinement details for $[Mn^{III}_3ScO_3]$

$[Mn^{III}_3ScO_3]$ was crystallized from C_6H_6/Et_2O mixture. The compound crystallized with two benzene and two diethyl ether solvent molecules in the lattice that were modeled successfully. Some constraints were employed to treat the displacement parameters of the atoms on some solvent molecules to an acceptable size. One of the benzenes solvents was disordered at two positions. An oxygen atom (O4) corresponding to the basal oxygen in the cubane motif in starting **$[Mn^{III}Mn^{IV}_2ScO_4]$** was modeled with 15% occupancy (85% occupancy of **$[Mn^{III}_3ScO_3]$**). The 15% occupancy of O4 may have come from co-crystallized starting material or uptake of oxygen atom from the air upon crystal handling/mounting.

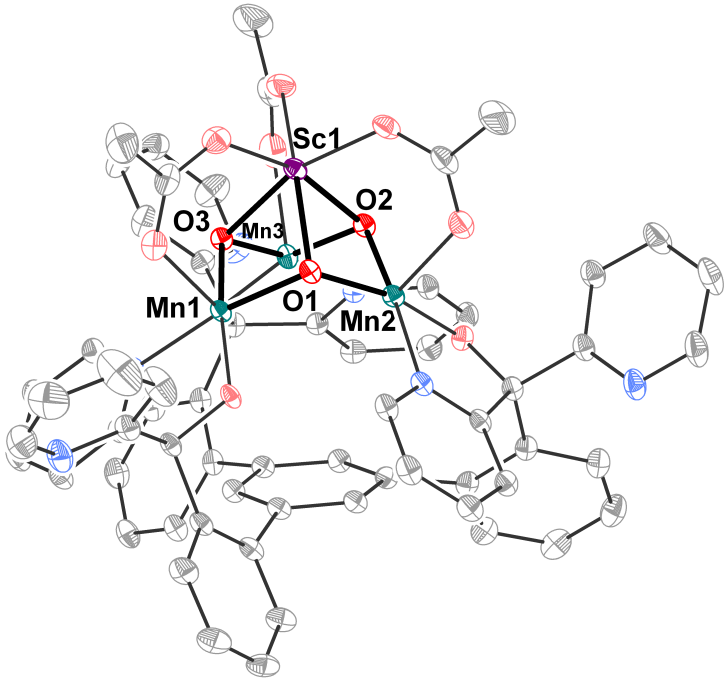

Figure S23. Solid-state structure of **$[Mn^{III}_3ScO_3]$** as 50% thermal ellipsoids. Hydrogen atoms and solvent molecules are omitted for clarity.

Optimized Geometries for Calculated Complexes.
The following color scheme is employed: Ca (silver), C (brown), H (green) O (red), F (pink), N (baby blue), S (orange).

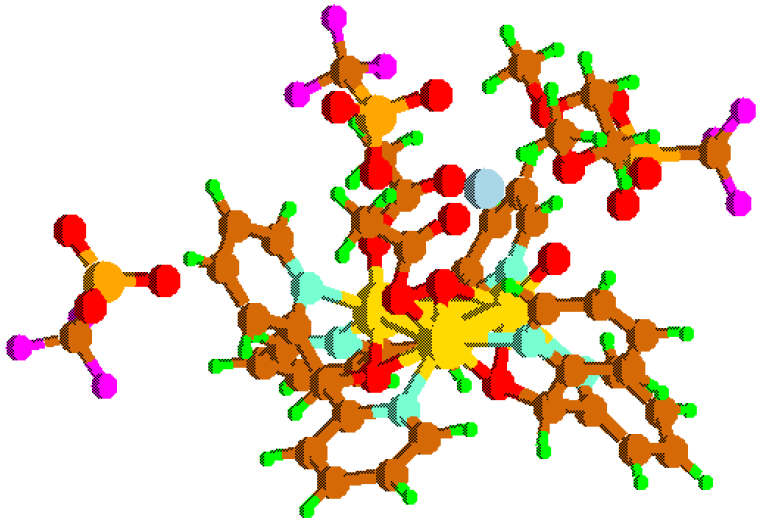

Figure S24. Optimized Structure of **oxCa'**.

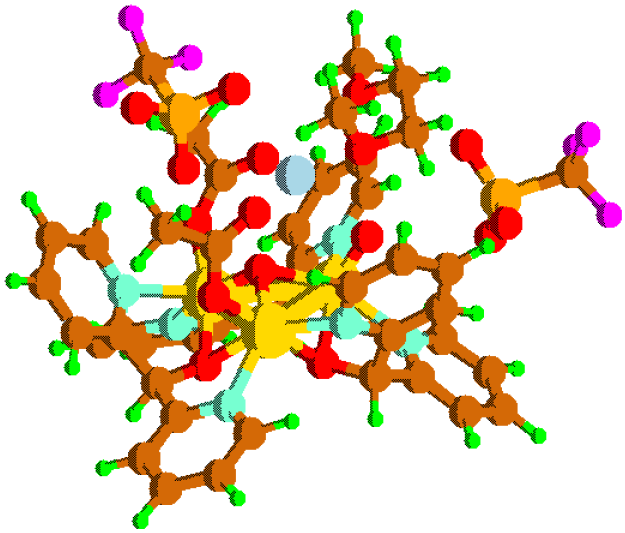

Figure S25. Optimized structure of **redCa'**

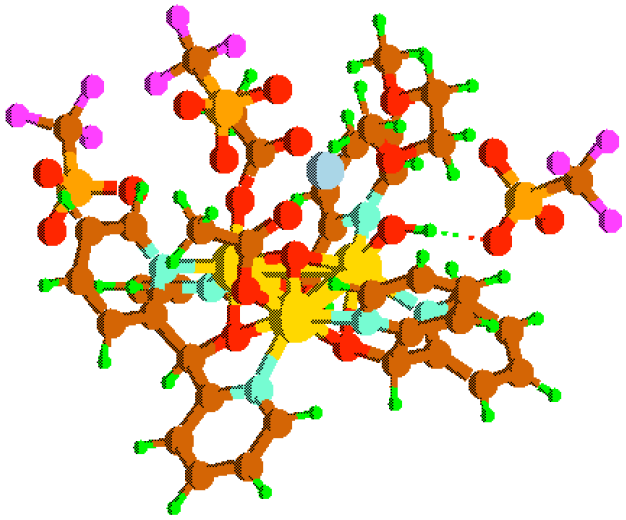

Figure S26. Optimized structure of **oxCa"**

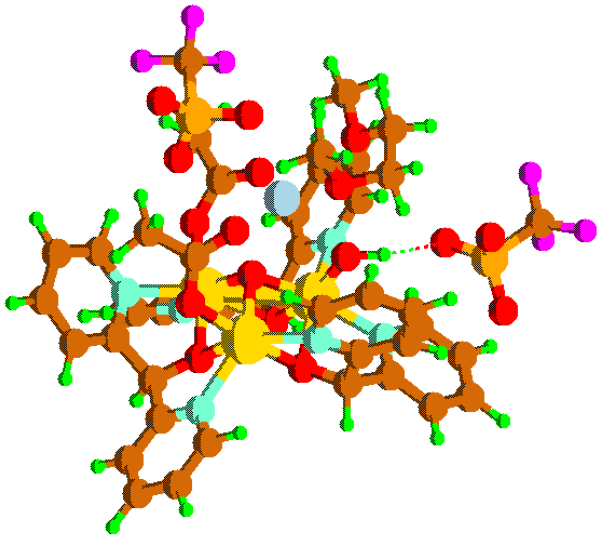

Figure S27. Optimized structure of **redCa"** (H-bonding between triflate and hydroxide ligand)

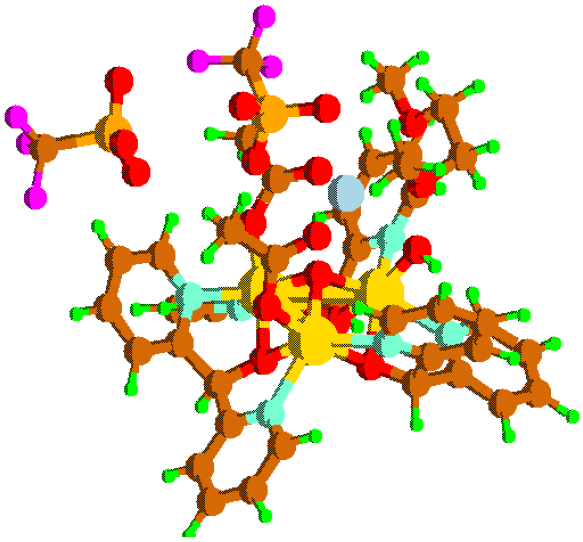

Figure S28. Optimized structure of **redCa"-noH** (no H-bonding between triflate and hydroxide ligand)

References

1. Tsui, E. Y.; Tran, R.; Yano, J.; Agapie, T. Redox-inactive metals modulate the reduction potential in heterometallic manganese-oxido clusters. *Nat. Chem.* **2013,** *5*, 293-299 DOI: 10.1038/Nchem.1578.
2. Herbert, D. E.; Lionetti, D.; Rittle, J.; Agapie, T. Heterometallic Triiron-Oxo/Hydroxo Clusters: Effect of Redox-Inactive Metals. *J. Am. Chem. Soc.* **2013,** *135*, 19075-19078 DOI: 10.1021/Ja4104974.
3. Bochevarov, A. D.; Harder, E.; Hughes, T. F.; Greenwood, J. R.; Braden, D. A.; Philipp, D. M.; Rinaldo, D.; Halls, M. D.; Zhang, J.; Friesner, R. A. Jaguar: A high-performance quantum chemistry software program with strengths in life and materials sciences. *Int. J. Quantum Chem.* **2013,** *113*, 2110-2142 DOI: 10.1002/qua.24481.
4. Kanady, J. S.; Tsui, E. Y.; Day, M. W.; Agapie, T. A Synthetic Model of the Mn3Ca Subsite of the Oxygen-Evolving Complex in Photosystem II. *Science* **2011,** *333*, 733-736 DOI: 10.1126/Science.1206036.
5. Kakuda, S.; Peterson, R. L.; Ohkubo, K.; Karlin, K. D.; Fukuzumi, S. Enhanced Catalytic Four-Electron Dioxygen (O-2) and Two-Electron Hydrogen Peroxide (H2O2) Reduction with a Copper(II) Complex Possessing a Pendant Ligand Pivalamido Group. *J. Am. Chem. Soc.* **2013,** *135*, 6513-6522 DOI: 10.1021/Ja3125977.
6. Sheldrick, G. M. *Program for Absorption Correction for Data from Area Detector Frames*, 2008/1; University of Göttingen, Germany: 2008.
7. Chen, J.; Lee, Y. M.; Davis, K. M.; Wu, X.; Seo, M. S.; Cho, K. B.; Yoon, H.; Park, Y. J.; Fukuzumi, S.; Pushkar, Y. N.; Nam, W. A Mononuclear Non-Heme Manganese(IV)-Oxo Complex Binding Redox-Inactive Metal Ions. *J. Am. Chem. Soc.* **2013,** *135*, 6388-6391 DOI: 10.1021/Ja312113p.
8. Sheldrick, G. M. A Short History of *SHELX*. *Acta Crystallogr. A* **2008,** *D65(2)*, 148-155.